OPEN ACCESS TECHNICAL REPORT

Bragg Coherent Imaging of Fluctuating Domains

IAN K. ROBINSON
London Centre for Nanotechnology, University College London, London, UK; Condensed Matter Physics and Materials Science, Brookhaven National Laboratory, Upton NY, USA

This review presents two examples of domain dynamics in crystalline solid state samples which were imaged recently with synchrotron X-rays by Bragg Coherent Diffraction methods. Domains are associated with sub-atomic phase shifts in the structure which are revealed by the strong phase contrast associated with Bragg diffraction. At low temperatures, $La_{2-x}Sr_xNiO_4$ has an antiferromagnetic spin-ordered phase with correlation lengths of 200 nm; its domains are imaged with magnetic Bragg Ptychography to visualize their slow fluctuations. Hydrothermally synthesized nanocrystalline $BaTiO_3$ is found to be made up of ~50 nm domains using Bragg Coherent Diffraction Imaging; electric field induced movement of its internal domain walls is a likely explanation of the nano-material's anomalously large dielectric constant, which is used in the manufacture of multilayer ceramic capacitors.

In condensed matter physics, domains of crystalline order mediate a number of material properties, including transport. The domains can fluctuate spontaneously near phase transitions or migrate under external fields. X-ray scattering measurements are one of the main methods of studying the average domain sizes and their distribution. Coherent X-ray methods, the focus of this review, offer powerful ways of imaging their structures in 3D. Domains lie at the heart of our understanding, not only of phase transitions, but the properties of ferroelectric and magnetic materials, as we illustrate here.

To image domains with X-rays, it is important to make use of coherent Bragg diffraction methods because they would often be invisible otherwise. This is illustrated in Figure 1, which defines a domain structure with respect to a reference lattice; in the case of epitaxial misfit domains, this might be the substrate, but otherwise it would be some average lattice. The sensitivity to domains is the same as sensitivity to strain [1] and, by analogy, the image phase is a projection onto the momentum transfer vector, **Q**. This means some domain boundaries are rendered invisible, when they happen to have the same projection. Coherence is required so that the interference between adjacent domains is established. The domain walls, boundaries separating the domains, are not directly visible, but their structure can be inferred from the relative phase shift between domains.

The two coherent diffraction methods discussed here are Bragg Coherent Diffractive Imaging (BCDI) and Bragg Ptychography. Both make use of a coherent X-ray beam, supplied by a synchrotron radiation source, usually an X-ray undulator, made longitudinally coherent by use of a monochromator and transversely coherent with slits. At the latest multibend achromat synchrotron radiation sources, this can have a flux approaching 10^9 photons per second. This beam is usually focused or collimated to a small "probe" beam around 1 micron in size which impinges on the sample and the diffraction is measured with a fine-pixel area detector placed at the Bragg angle. BCDI operates in the limit where the sample is smaller than the beam, so it is used to study crystalline nanoparticles. Here, the resulting diffraction pattern is strongly modulated by interference between the sample boundaries, resulting in a distinct pattern of fringes. The detector, at a distance D, must be far enough away to "oversample" the recording of the fringes, usually with at least two pixels per fringe. The optical diffraction formula for the fringe spacing, $s = \lambda D/d$, for a sample size d, is used to achieve this. 3D diffraction patterns are routinely measured by rocking the sample through its Bragg peak with a step size small enough to achieve oversampling. Since rocking curves are typically less than 1 degree wide, most BCDI instruments have no trouble keeping the sample in the beam.

The BCDI image of the sample is a complex density function in which the amplitude measures the nominal electron density and the phase measures the local displacement of each region, as defined in Figure 1. In the single scattering limit, the X-ray diffraction pattern seen on the detector is given by the 3D Fourier transform of this complex density. If this were fully recorded, the 3D image of the sample could be trivially reproduced with an inverse Fourier transform. However, all current X-ray detectors measure only the intensity, which is the square magnitude of this signal, and lose the phase information. This results in a "phase problem" to solve before the 3D image can be generated.

Fortunately, as pointed out by Sayre [2], so long as the diffraction pattern is oversampled (as defined by Nyquist-Shannon information theory [3]), the problem is mathematically overdetermined. A long list of successful inversion algorithms has proved successful in solving the BCDI phase problem, of which the most important is Fienup's hybrid input-output method [4] and, recently, Machine Learning [5, 6].

Bragg Ptychography, on the other hand, operates in the limit where the sample is larger than the beam, so is used to study extended samples. It is an extension to the Bragg diffraction situation of classical in-line ptychography, originally attributed to Walter Hoppe [7], and developed for X-rays by the pioneering work of John Rodenburg [8] and Franz Pfeiffer [9]. The coherent probe is scanned in an array of overlapping positions on the sample and the diffraction patterns are collected. The diffraction pattern is assumed to be the Fourier transform of the

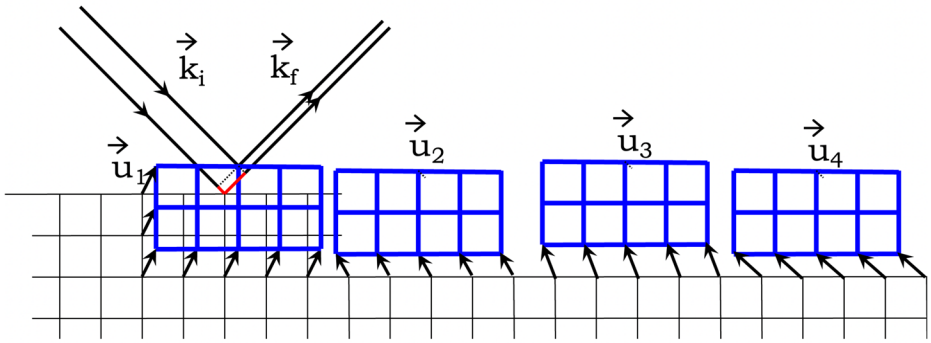

Figure 1: Sensitivity of coherent diffraction methods to domains, represented as blocks of crystal displaced relative to a reference lattice. The relative phase of both the incident and exit wavevectors, $\boldsymbol{k}_i$ and $\boldsymbol{k}_f$, are shifted by the displacement vector of the block, $\boldsymbol{u}_1$. This results in a region which is phase shifted in the image by $\Delta\varphi = \boldsymbol{k}_f\boldsymbol{u}_1 - \boldsymbol{k}_i\boldsymbol{u}_1 = \boldsymbol{Q}.\boldsymbol{u}_1$. Multiple domains, represented by different displacements, $\boldsymbol{u}_i$, show up with different phases, $\Delta\varphi_i = \boldsymbol{Q}.\boldsymbol{u}_i$.

probe multiplied by that of the sample transmission function, both assumed complex. The redundancy of each point on the sample being measured multiple times means there is enough information both to solve the aforementioned phase problem of the diffraction but also to separate the sample and probe functions cleanly. A number of powerful algorithms have been developed which show strong convergence to a unique solution, including corrections for probe-position errors and partial beam coherence [8, 9].

An analogous situation applies when the probe undergoes Bragg diffraction from the sample with the additional advantage that the image phase includes the contribution of the domains present on the sample. Bragg Ptychography becomes complicated when the beam divergence exceeds the rocking curve width because the probe position changes whenever the sample is rocked, but this problem has been solved in the work published to date [10, 11]. In the next section of this review, we discuss an example where the penetrated region of the sample is so thin that the diffraction extends far enough that the Ewald sphere cuts across it completely, so that it can be fully measured with just a 2D raster scan, which avoids the rocking problem.

Imaging of magnetic domains in $La_{2-x}Sr_xNiO_4$

Strong correlations in transition metal oxides between charge, spin, orbital, and lattice degrees of freedom can lead to the emergence of symmetry-breaking novel quantum states, such as spin order (SO), charge order (CO), and superconductivity [12, 13]. Within these states, electrons exhibit collective behavior, and their corresponding dynamics are often represented in the energy domain [14, 15]. Therefore, understanding the driving forces behind the formation of SO and CO "stripe" states and their dynamics is crucial to understanding their unconventional superconductivity [13]. However, due to the complex interplay between spin, charge, orbital, and lattice degrees of freedom, the microscopic mechanisms underlying these collective behaviors are mostly unknown and not captured well by theories based on effective single-electron interactions [16]. Stripe-ordered $La_{2-x}Sr_xNiO_4$ (LSNO) has received much attention due to its being a close analogue of the high-Tc cuprate superconductors [12, 17]. As a member of the (non superconducting) 214 nickelate family, LSNO was chosen for its complex interplay between spin-charge-lattice degrees of freedom. It exhibits distinct spin and lattice ordering into domains with only weak screening of low energy excitations [17–20]. X-ray photon correlation spectroscopy (XPCS) measurements had previously shown slow fluctuations particularly of SO stripes in LSNO [21, 22]. The time constant of the SO stripe fluctuations was found to vary significantly with temperature and was slowest at T ~70 K where we performed the experiment.

To image the magnetic domain structures, we exploited Bragg ptychography, using the phase contrast arising from the domain positions, as explained in Figure 1. Technically, the soft X-ray version of the experiment is challenging because of parasitic scattering of the optics, which took several attempts to rectify. The resonant soft x-ray ptychography experiments were performed at the CSX beamline of NSLS-II at the Ni L_3 edge at 852 eV using π polarization, which greatly enhances the magnetic diffraction signal. The sample was mounted on a heavy cryostat which could not be scanned, so we scanned the coherence-defining pinhole instead. As shown in the geometry of Figure 2(a), the SO peak was close to backscattering and the X-ray penetration was less than one domain, in which geometry the raster scan maps the lateral domain structure as a single 2D layer. To reduce the parasitic scattering, a Focused Ion Beam (FIB) was used to polish the inside surface of the coherence-defining entrance pinhole. This turned out to be essential to the success of the experiment. Significantly, the "thin-film" geometry of Figure 2 favors 2D imaging without any changes in the sample angle.

The final innovation was to modify the standard in-line ptychography algorithm [9] to work with the geometry of Figure 2. We chose to perform the reconstruction in the detector coordinate system, which is roughly perpendicular to the face of the sample. This first required accurately transforming the array of probe positions from the scanner frame to the detector frame. The initial estimate of the probe was similarly transformed and the reconstruction was found to converge; small corrections to the probe posi-

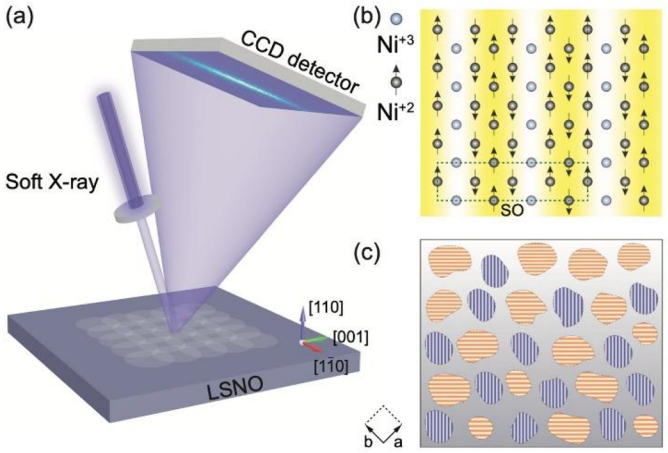

Figure 2: (a) Schematic experimental soft X-ray Bragg ptychography experimental setup. (b) Cartoon of the spin stripe order in nickelate with simplified ionic doping level $x = 0.25$. The doped holes reside on Ni and neighboring O ions, resulting in effective Ni^{3+} ions. The remaining Ni^{2+} ions are at high-spin state ($S = 1$). SO labels the unit cell of the spin superstructure and the shading shows the charge density distribution. (c) Schematic showing SO stripe domains with different modulation directions in the NiO_2 square plane.

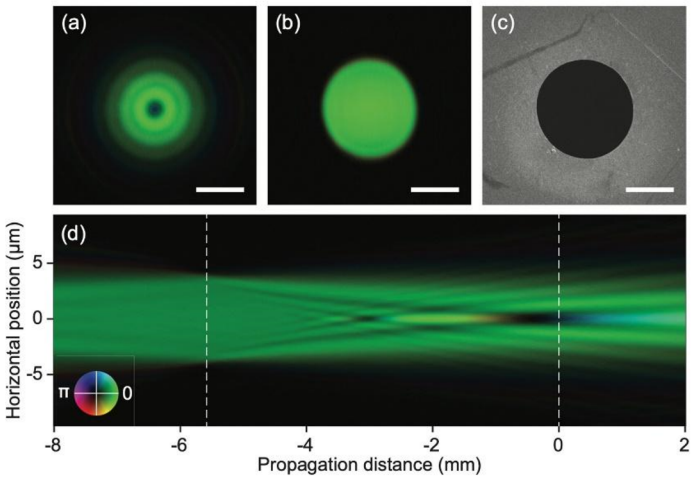

Figure 3: Phase propagation of the beam profile defined by the FIB-polished pinhole. (a) Profile at the sample position, as measured in the ptychography experiment. (b) Propagation to the pinhole plane. (c) SEM image of the polished pinhole. (d) Cross section of the profile as a function of propagation distance. Scale bar is 4 microns.

tions were needed too. Finally, the reconstructed probe wavefront was transformed back to the lab frame and the resulting sample image was transformed onto the flat [110] face of the sample. The need for all these coordinate transformations can clearly be seen in Figure 2.

The clean separation of the probe and sample images is a valuable feature of ptychography. In our LSNO experiment, the "probe," the pinhole-defined illumination wavefront, shown in Figure 3, was accurately measured along with the image of the sample, which is shown in Figure 4 [23]. Because the probe is fully measured as a complex function, it can be Fresnel propagated to any other plane. A propagation by 5.57 mm to the physical pinhole plane is shown in Figure 3(b), where the sharp FIB-polished edges of the pinhole can clearly be seen to agree with the SEM image in Figure 3(c). A side view of the full evolution of the wavefield of the circular aperture, shown in Figure 3(d), shows the development of an "Arago dark spot" [24] which we see directly in the reconstructed image, Figure 3(a).

The ptychography images in Figure 4 are very striking and clearly interpreted as phase domains. Clear scratches, containing no SO domains, were also seen which were due to the mechanical sample polishing. These were used as fiducials to control the exact location of the domain-filled region seen on the sample in Figure 4. We can see that the spin-ordered domains of LSNO are phase shifted with respect to each other. They could be imaged faster than their slow dynamics. Temporal fluctuations were seen between the frames, but only in the amplitudes of the domains, not their phase, suggesting the domains are pinned, possibly by the preparation scratches. It seems that this mechanism represents a different origin of the XPCS fluctuations from the usual interpretation due to Brownian motion common in colloids [25]. Brownian motion leads to a distinct Q-dependence of the XPCS signal, whereas in Bragg XPCS of LSNO none was detected [22].

BCDI of nanostructured dielectrics

In the future, we would like to perform BCDI experiments [1] *in-situ* under applied electric fields to understand the involvement of domains dynamics in the dielectric properties of ferroelectric materials. BCDI has seen powerful applications for imaging strains which appear during *operando* studies of active catalyst particles [26] and live coin-cell battery assemblies [27], direct electric-field induced strains in dielectric materials have yet to be achieved by this method until now.

We performed a BCDI study of nanocrystalline $BaTiO_3$ (BTO) particles [28] made by hydrothermal synthesis, similar to those widely used as the dielectric material in multilayer ceramic capacitor (MLCC) technology. The low temperatures involved lead to not only nanoscale particle sizes, but also significant disorder which can be imaged as strain. The nano BTO is commercially important because it is found to have a several-fold enhanced dielectric constant, exceeding 6000 [29] which has been widely utilized to manufacture MLCC capacitors. Several models have been proposed over the years for this enhanced dielectric behavior at small particle size, including core-shell structures [30, 31], Ba^{2+} vacancies and incorporation of hydroxyl ions into the crystalline lattice [32] or a "critical size" effect for cubic symmetry [33], analogous to favoring anatase over rutile for nanoparticles of TiO_2 [34].

These nano-BTO materials are commonly considered to consist of either a single cubic average structural phase or a mixture of cubic and tetragonal phases. By combining powder diffraction at APS beamline

11-BM and BCDI methods at APS 34-ID-C, we demonstrated that the material has local structural symmetry breaking throughout its structure and that its apparent cubic long-range symmetry arises from ~50 nm twin domains which interact to give the net cubic structure and residual strain [28]. In Figure 5(e), we model the structure of the cubic-phase BTO nanoparticles as close-packed side-by-side domains with 90° domain walls [28]. Comparing cubic and tetragonal preparation routes giving similar particle size, we find the cubic particles show stronger "microstrain" in the Williamson-Hall analysis of powder diffraction [35]. When imaged with BCDI, we find individual nanoparticles invariably contain multiple domains with spatially varying strain inside. In Figure 5 we show an example of a strong phase variation in a cross-sectional slice, seen in a map of the 110-component of the local lattice displacement as a color variation. This can be accurately explained as side-by-side merohedral twin domains ("90° domains") joined along their {101} planes as shown in Figure 5(e) [36]. The line

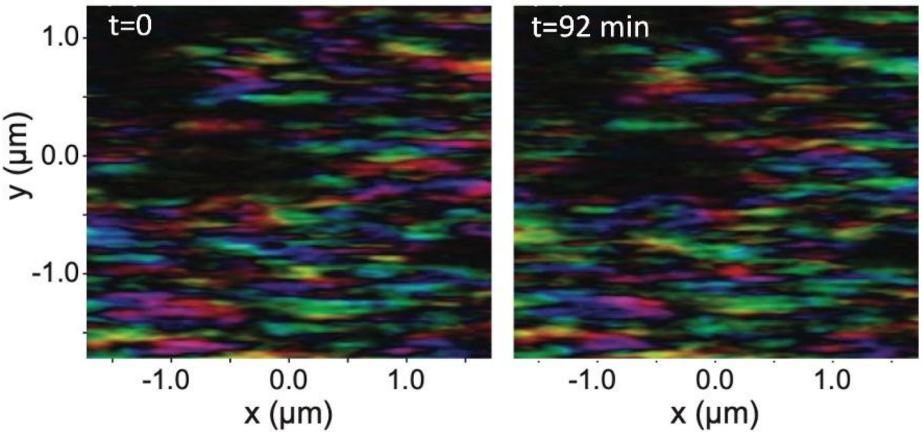

Figure 4: Phase contrast images of the SO domains recorded from the LSNO sample at two times. The phase, encoded by color, indicates the domain position relative to the underlying crystal. Small changes of amplitude were detected as a function of time, suggesting growth and shrinking of the domains, but not a change in their relative positions.

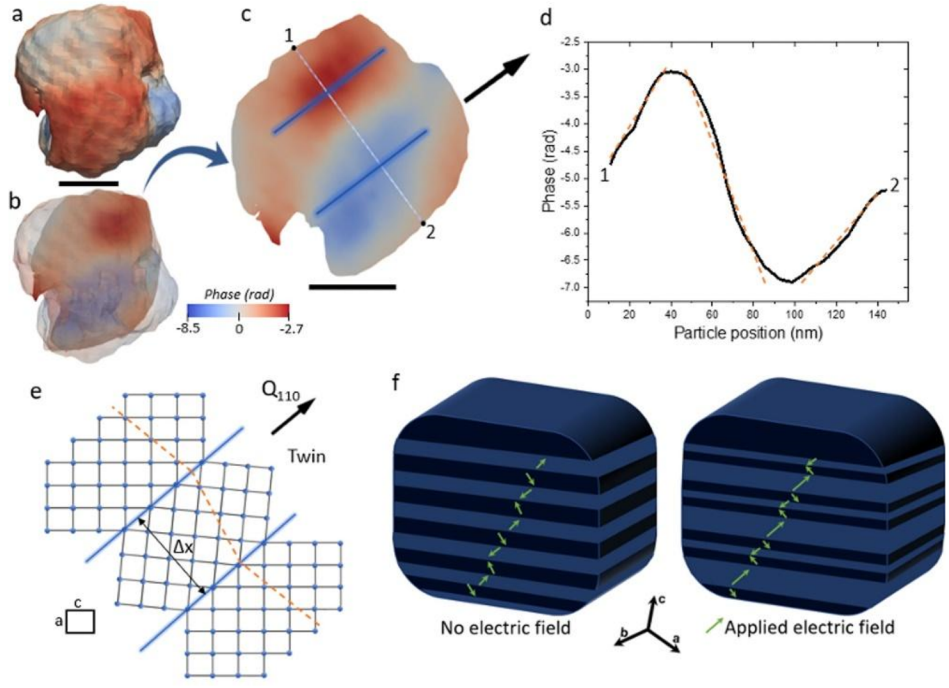

Figure 5: Isosurface (a) and cross-section slice (b,c) through a cubic BTO nanoparticle. The color indicates local displacement from a reference lattice on a scale of 2π rad = d_{110}. Line section (d) agrees with merohedral twinning of tetragonal domains meeting at {110} domain boundaries.

scan across the assembly, perpendicular to the Q-vector, sees a V-shaped ramped phase structure resulting in a lattice offset, which agrees well with the model. The resulting particle is cubic on average because of this strain, while the domains are locally tetragonal with their c-axes oriented in different directions, consistent with the PDF. The BCDI images, shown in Figure 5(f), support a model of facile domain wall migration in response to an electric field which needs to be tested. If confirmed, this model could resolve the longstanding question of why nano-$BaTiO_3$ has a strongly enhanced dielectric constant [29], with important device applications in MLCCs.

One way to test the hydrothermal BTO nanoparticles in the presence of electric fields up to several MV/m, is to assemble them on lithographic electrode arrays. We would drop-cast the particles onto gold interdigital electrode arrays with few-micron electrode spacing, following the approach of Kim et al [37]. Tetraethyl Orthosilicate (TEOS), followed by calcining in air, can then be used to bond the particles hermetically [38] into a continuous film to avoid dielectric leakage of the electric field between the dielectric particles. The capacitance increment of the assembled devices can be used to assess the quality of the contacts [36]. Another approach would be to look directly inside commercial MLCC capacitors, which use the X5R dielectric, containing 90–98% BTO nanoparticles [39]. The BTO grain size within these commercial X5R-based MLCCs is reported to be 240 nm [40], which is perfect for BCDI experiments. The c-axis is the polarization axis of the tetragonal ferroelectric phase of BTO. Our model of dielectric enhancement in Figure 5(f) is that the cubic nanoparticles contain domains with the c-axis locally pointing in different directions, as seen with BCDI. When we apply an electric field to the particle, the domains may suddenly reorient (and generate hysteresis), but it is also possible that the domains pointing in the direction of the field will grow continuously and the others will shrink, as illustrated in Figure 5(f). This would explain the enhanced dielectric behavior of the cubic nanoparticles. It would also explain the long service lifetimes and excellent high frequency performance of the widely-used commercial nano-BTO thin-layer MLCC's. In these future experiments, the domain structures will be imaged in 3D using BCDI, while the electric fields are changed *in-situ*.

Future outlook

Many of the world's Synchrotron Radiation facilities are considering "upgrades" of their magnetic lattices to multibend achromat designs, which will reduce their emittance by about a factor of 100. This is often justified because the undulator brightness gain can be directly seen in the available coherent flux. All coherent imaging experiments, CDI, BCDI, ptychography and Bragg ptychography, as well as XPCS, can benefit from this gain and so are likely to become more powerful in the future. This editorial has focused on the use of Bragg diffraction to image crystal distortions, generally as projections of strain fields, but specifically here for imaging phase domains in crystalline materials. The domain fluctuations we have discussed, either spontaneous as in LSNO, or driven as in BTO, can in principle then be studied on much faster time scales.

Acknowledgments

The work on $BaTiO_3$ was performed in collaboration with Ana Suzana, Wonsuk Cha and Ross Harder; the measurements were carried out at the Advanced Photon Source (APS) beamlines 34-ID-C and 11-BM, which were supported by the U. S. Department of Energy, Office of Science, Office of Basic Energy Sciences, under Contract No. DE-AC02-06CH11357. The beamline 34-ID-C was originally built with the help of U.S. National Science Foundation grant DMR-9724294. The work on $La_2-xSrxNiO_4$ was carried out in collaboration with Longlong Wu and Claudio Mazzoli; the measurements made use of the 23-ID-1 beamline of the National Synchrotron Light Source II, a U.S. DOE Office of Science User Facility. Work at Brookhaven National Laboratory was supported by the U.S. Department of Energy, Office of Science, Office of Basic Energy Sciences, under Contract No. DE-SC0012704. Work performed at UCL was supported by EPSRC.

Disclosure statement

No potential conflict of interest was reported by the authors. ■

References

1. I. Robinson and R. Harder, *Nature Mater.* **8**, 291 (2009). doi:10.1038/nmat2400
2. D. Sayre, *Acta Cryst.* **5**, 843 (1952). doi:10.1107/S0365110X52002276
3. C. E. Shannon, *Bell Syst. Techn. J. XXVII* **27**, 379 (1948).
4. J. R. Fienup, *Opt. Lett.* **3**, 27 (1978). doi:10.1364/OL.3.000027
5. L. Wu et al., *IUCrJ* **8**, 12 (2021). doi:10.1107/S2052252520013780
6. L. Wu et al., *Npj Comput. Mater.* **7** (2021). doi:10.1038/s41524-021-00644-z
7. W. Hoppe, *Acta Cryst. A.* **25**, 508 (1969). doi:10.1107/S0567739469001069
8. J. M. Rodenburg et al., *Phys. Rev. Lett.* **98**, 034801 (2007). doi:10.1103/PhysRevLett.98.034801
9. F. Pfeiffer, *Nature Photon.* **12**, 9 (2018). doi:10.1038/s41566-017-0072-5
10. S. O. Hruszkewycz et al., *Nature Mater.* **16**, 244 (2017). doi:10.1038/nmat4798
11. P. Li et al., *Nat. Commun.* **12**, 7059 (2021). doi:10.1038/s41467-021-27224-5
12. D. F. Agterberg et al., *Annu. Rev. Condens. Matter Phys.* **11**, 231 (2020). doi:10.1146/annurev-conmatphys-031119-050711
13. R. Comin and A. Damascelli, *Annu. Rev. Condens. Matter Phys.* **7**, 369 (2016). doi:10.1146/annurev-conmatphys-031115-011401
14. J. M. Tranquada, P. Wochner, and D. J. Buttrey, *Phys. Rev. Lett.* **79**, 2133 (1997). doi:10.1103/PhysRevLett.79.2133
15. G. Fabbris et al., *Phys. Rev. Lett.* **118**, 156402 (2017). doi:10.1103/PhysRevLett.118.156402
16. T. Hotta and E. Dagotto, *Phys. Rev. Lett.* **92**, 227201 (2004). doi:10.1103/PhysRevLett.92.227201
17. J. M. Tranquada et al., *Nature* **375**, 561 (1995). doi:10.1038/375561a0
18. M. Filippi et al., *J. Appl. Phys.* **106**, 104116 (2009).
19. C. H. Chen, S. W. Cheong, and A. S. Cooper, *Phys. Rev. Lett.* **71**, 2461 (1993). doi:10.1103/PhysRevLett.71.2461
20. S. M. Hayden et al., *Phys. Rev. Lett.* **68**, 1061 (1992). doi:10.1103/PhysRevLett.68.1061
21. S. Yamamoto, T. Fujiwara, and Y. Hatsugai, *Phys. Rev. B.* **76**, 165114 (2007). doi:10.1103/PhysRevB.76.165114
22. Y. Shen et al., *Phys. Rev. Lett.* **126**, 177601 (2021). doi:10.1103/PhysRevLett.126.177601

23. L. Wu et al., *Phys. Rev. Lett.* **127**, 275301 (2021). doi:10.1103/PhysRevLett.127.275301
24. J. E. Harvey and J. L. Forgham, *Amer. J. Phys.* **52**, 243 (1984). doi:10.1119/1.13681
25. S. B. Dierker et al., *Phys. Rev. Lett.* **75**, 449 (1995). doi:10.1103/PhysRevLett.75.449
26. A. Ulvestad et al., *Science* **348**, 1344 (2015). doi:10.1126/science.aaa1313
27. A. Ulvestad et al., *J. Phys. Chem. Lett.* **7**, 3008–3013 (2016). doi:10.1021/acs.jpclett.6b01038
28. A. F. Suzana et al., *Adv. Funct. Mater.* **33**, 2208012 (2023). doi:10.1002/adfm.202208012
29. L. Curecheriu et al., *Appl. Phys. Lett.* **97**, 1 (2010).
30. T. Hoshina et al., *Appl. Phys. Lett.* **93**, 2006 (2008).
31. Z. Tian et al., *J. Am. Ceram. Soc.* **94**, 973 (2011). doi:10.1111/j.1551-2916.2010.04357.x
32. R. Vivekanandan and T. R. N. Kutty, *Powder Technol.* **57**, 181 (1989). doi:10.1016/0032-5910(89)80074-9
33. M. Frey and D. Payne, *Phys. Rev. B.* **54**, 3158 (1996). doi:10.1103/PhysRevB.54.3158
34. H. Zhang and J. F. Banfield, *J. Mater. Chem.* **8**, 2073 (1998). doi:10.1039/a802619j
35. G. K. Williamson and W. H. Hall, *Acta Metall.* **1**, 22 (1953). doi:10.1016/0001-6160(53)90006-6
36. D. Ghosh et al., *Adv. Funct. Material.* **24**, 885 (2014). doi:10.1002/adfm.201301913
37. E.-S. Kim et al., *Sci. Rep.* **9**, 680 (2019). doi:10.1038/s41598-018-37416-7
38. M. Monteforte et al., *J. Synchrotron Rad.* **23**, 953 (2016). doi:10.1107/S1600577516006408
39. D.-H. Yoon, *J. Ceramic Process. Res.* **7**, 343 (2006).
40. J. Kunlun et al., *Ceram. Int.* **48**, 30020 (2022).